NON-PEER-REVIEWED PREPRINT

Calibrated detection limits in routine Sentinel-1 products 50.6 hours before the Langtang Lirung rock–ice avalanche, Nepal

Ajay Kumar Sah
Purbanchal University School of Engineering, Biratnagar, Nepal
ajayshah2005@gmail.com
ORCID: https://orcid.org/0009-0004-8543-4306

Companion to: Sah, A. K. (2026) No detectable precursor in Sentinel-1 backscatter before the 26 August 2026 Langtang Lirung rock–ice avalanche, Nepal. EarthArXiv, doi:10.31223/X59N5N

Supplementary data, analysis code and derived figures are archived at Zenodo, doi:10.5281/zenodo.22676918

Prepared 9 September 2026.

Abstract

On 26 August 2026 a rock–ice avalanche detached from Langtang Lirung, Nepal, and released a debris flood that crossed the Nepal–China border. Deformation preceding the failure has since been reported from a multi-month Sentinel-1 stack, and pre-event indications have been identified in commercial optical imagery. Both analyses began from a known failure location. This paper asks a different question: what routine, freely available Sentinel-1 products contained at the last acquisition before failure, and how large a signal would have had to be before they contained something. Three quantities are tested on a 500 m disc over the detachment — backscatter amplitude, interferometric coherence, and line-of-sight displacement from unwrapped phase — each against 120 control discs in the same scene matched on local incidence angle, aspect and slope, and against the source's own history over the preceding two months. The last usable descending acquisition precedes failure by 50.6 hours. No quantity distinguishes the source from comparable slopes or from its own quiet behaviour: amplitude at the 67.5th percentile of controls, coherence third of five quiet intervals, cumulative displacement at the 31st percentile. The same statistics identify the collapse decisively once it falls inside the observation interval, at $z = 4.57$ in coherence and below all 120 controls in amplitude, so these are calibrated limits rather than uninformative nulls. No surface disturbance above approximately 2 ha of coherent decorrelation occurred in the twelve days ending 50.6 hours before failure, and no line-of-sight displacement above approximately 13 mm per month occurred over the preceding seven weeks. That bound lies above the rate reported from the multi-month stack, which is the substantive result: the deformation was measurable from orbit using free archived data, but not by the twelve-day products a monitoring service would have been screening.

Keywords: Sentinel-1, InSAR coherence, detection limits, rock–ice avalanche, early warning, Himalaya, Langtang, Nepal

---

1. Introduction

At 02:52:10 UTC on 26 August 2026 — 08:37:10 Nepal Standard Time, on a clear morning — a mass of rock and ice detached from Langtang Lirung, Nepal, at approximately 5,100 to 5,200 m, fell into the Lhende Khola, and released a debris flood that travelled through the Bhote Koshi and Trishuli network, destroying the Rasuwagadhi border crossing and a corridor of infrastructure downstream. As of 18:00 on 9 September 2026 the National Disaster Risk Reduction and Management Authority reported 1,369 deaths and 5,132 people missing in Nepal, the missing figure net of 102 bodies since identified, together with 13,646 rescued and 21,185 security personnel mobilised; a further 16 deaths were reported on the Chinese side of the border (NDRRMA, 2026). The toll was still rising as this was written: the same authority gave 1,114 dead and 3,916 missing a week earlier, on 2 September. The seismic signal, catalogued by the USGS as us7000tbwb at M5.2, was initially attributed to an earthquake and subsequently reclassified as a mass movement; the catalogue entry carries the magnitude type ms_vx, a surface-wave variant used for non-tectonic sources, and a depth fixed at zero. A second discrete event, us7000tc90 at M4.2, followed 3.14 hours later, so post-event imagery records the sum of both. A search of the ANSS Comprehensive Catalog over a region spanning the Nepal–China border for the thirty days preceding failure returns these two entries and no others; both are classified as landslides rather than earthquakes. No tectonic earthquake is recorded in that window, and a seismic trigger is therefore excluded down to the catalogue's practical completeness in Nepal, around magnitude 4 to 4.5. Smaller local events remain untested, since detection at that level requires the national network rather than the global composite.

The sequence belongs to a class of geomorphic process chains, in which a failure at high elevation entrains further material and transforms as it travels, reviewed and classified for hazard assessment by Mani et al. (2023). The remote sensing capability available for observing such chains across High Mountain Asia was surveyed by Kirschbaum et al. (2019). What follows is a quantitative instance of that survey applied to a single event, and to the particular products that were in hand before it.

The question that followed immediately, in the scientific press and in Nepal, was whether the collapse could have been anticipated. Slow downhill movement of the rock and ice near the failure area, reaching roughly 10 mm per month, has since been reported from an eight-month Sentinel-1 stack spanning 8 January to 18 August 2026, the last acquisition preceding failure by about a week (Shirzaei, interviewed in Basu, 2026). That analysis is not peer reviewed, no time series has been published, and its author describes the results as preliminary and subject to ruling out other possibilities. A rapid hazard assessment (HiRISK, 2026) has separately reported an ice surface speeding up toward the eventual failure location, meltwater visibly discoloured by 24 August, and some indication of a crack propagating into the surrounding bedrock, all identified explicitly in hindsight from Landsat 9 and Planet imagery. These results have been widely read as evidence that the warning signs were visible.

Whether a signal is visible in a retrospective multi-epoch inversion and whether it is visible in the products a monitoring service would have been holding at the time are separate questions, and only the second bears on early warning. This paper addresses the second. It asks what routine, freely available Sentinel-1 products contained at the last acquisition before failure, and — where they contained nothing — how large a signal would have had to be before they contained something.

A second difficulty attaches to every retrospective analysis of this event, and it is the one this study is designed to address. Cook has put the position plainly: warning signs can be identified after the fact, but only because the location where they should be sought is known afterwards, and the Himalaya is far too large to monitor in its entirety. Every analysis published so far began from a known failure location. Whether a signal is retrievable once the answer is known, and whether it would have been flagged by someone screening the region without that knowledge, are different propositions, and only the second describes an operational warning system.

The design used here separates them. Each measurement on the source is placed against 120 discs of the same size elsewhere in the same scene, matched on local incidence angle, aspect and slope, so that the question asked is not whether the source changed but whether it changed more than comparable slopes that did not fail. That is a test of whether the source would have stood out to an observer who did not already know where to look.

The approach is therefore to treat the source as one slope among many and as one interval among several. Three quantities are tested on a 500 m disc over the detachment: backscatter amplitude, interferometric coherence, and line-of-sight displacement from unwrapped phase. The last usable pre-event acquisition on the descending track is 24 August at 00:18 UTC, 50.6 hours before failure.

Two design choices distinguish this from a simple before-and-after comparison. First, every reported limit is calibrated: the same statistics are applied to the interval containing the collapse, so that a null before the event can be distinguished from a test with no power. Second, the results are reported as bounds rather than absences — the size of disturbance, and the rate of displacement, that would have exceeded normal variation.

This paper is a companion to Sah (2026), EarthArXiv 10.31223/X59N5N, which tested the amplitude record over the two months before failure on a single relative orbit against 80 terrain-matched control patches, locating the failure independently by change detection and rejecting a candidate cross-polarised trend as a delayed seasonal transition. The descending record examined here reaches 50.6 hours before the event, closer than that analysis allows, and adds the interferometric quantities that amplitude alone cannot provide. It is not the closest pre-event observation of any kind: Li (2026) report a usable

Sentinel-2 acquisition 45.85 hours before failure, showing no unambiguous large-scale surface change at 10 m sampling. The claim made here is specific to the radar record and to what interferometry can resolve. A spring snowpack climatology for the same region, which tests whether 2026 was anomalous in the months before failure, is reported in the Supplementary Material.

---

2. Data, geometry and study design

2.1 Acquisitions and products

All observations are Sentinel-1 C-band, descending, over an area of interest of 308 km^2 spanning 85.4458 to 85.6666 °E and 28.2230 to 28.3512 °N, with elevations from 2,426 to 7,180 m.

Acquisitions over this area fall into **three** interleaved twelve-day series, not one, and only two of them are descending. The ascending series at about 12:21 UTC, on 4, 16 and 28 August, carries the primary record of the companion amplitude study and is not used here. The two descending series are 7–19–31 August and 12–24 August–5 September, at about 00:10 and 00:18 UTC, corresponding to frames 499 and 497 and referred to here as track A and track B. The distinction between the two descending series is not cosmetic. Treating the six dates of these two descending series as a single time series introduces a spurious step on 24 August — the exact date under examination — because the two frames image the target from measurably different geometries. Mask intersection-over-union is 0.93 to 0.95 within a series and 0.827 to 0.830 across, and the separation is confirmed independently by granule metadata.

Interferometric products are six HyP3 INSAR_GAMMA pairs on track B, processed at 10 × 2 looks to 40 m pixels with the Copernicus GLO-30 digital elevation model included: five consecutive twelve-day pairs from 25 June to 24 August, and one 24-day pair from 12 August to 5 September that spans the failure.

Amplitude products are orthorectified terrain-flattened gamma-nought exports at 10 m from the Copernicus Data Space, on both tracks, converted to decibels.

Terrain geometry — local incidence angle, shadow mask and data mask — was exported separately for each track on a representative date, since these quantities are fixed per relative orbit. Slope, aspect and elevation are derived from the GLO-30 model supplied with the interferometric products, reprojected onto the geometry grid.

The last usable pre-event acquisition on track B is 24 August at 00:18 UTC, which precedes failure by 50.6 hours. On track A it is 19 August, 171 hours before.

No estimate of failure volume is adopted here, and none is needed. Published figures span three orders of magnitude and have not stabilised, ranging from 0.5–10 million m^3 for the initial mass through roughly 50 million m^3 to 100 million m^3 of rock plus tens of millions of ice. Mapped source area is better constrained but still definition-dependent: 1.009 km^2 for the changed surface, within envelopes of 0.491 to 1.841 km^2 (Li, 2026), against 0.72 km^2

for the detached ice–rock body from higher-resolution imagery (Guo et al., 2026). The difference reflects a changed-surface perimeter versus a detached body rather than a disagreement in measurement, and the two should not be merged. Maximum planimetric dimension is about 1,150 m, which exceeds the diameter of the analysis disc — a limit returned to in Section 2.4.

2.2 The source disc and the usable mask

The analysis disc is a circle of 500 m radius centred on 28.2853 °N, 85.5252 °E, containing 8,911 pixels on the 10 m geometry grid.

The disc is not uniformly observable. Its median local incidence angle on track B is 71.0°, close to grazing, and 24.6 per cent of it lies in radar shadow. Restricting to pixels with local incidence at or below 70° and outside shadow leaves 44.3 per cent of the disc. Intersecting further with the validity of all six interferometric products gives the working mask used throughout: n = 3,945 pixels, median local incidence 62.3°, circular-mean aspect 273°, median slope 33°, median elevation 5,000 m.

The westerly aspect is consistent across two elevation products and two independent delineations of the source. The GLO-30 model supplied with the interferometric products gives 273° on the disc used here and 280° on the disc centred on the alternative coordinate of Section 2.4; a separately obtained Copernicus 30 m tile gives 281°; and the source envelope mapped independently by Li (2026) gives 280.8°, with 48.2 per cent of its area west-facing and 33.8 per cent north-west-facing. These are not four independent measurements — the first two share a digital elevation model, and Li's mapping also derives orientation from Copernicus GLO-30 — but the agreement spans two products and two separate delineations of where the source lies.

An apparent conflict with other accounts is resolved by distinguishing two claims. Guo et al. (2026) place the source on the northern flank of Langtang Lirung, and a national situation report describes a north-facing slope. The first of these is a statement about position on the massif and is correct; the second is a statement about slope orientation and is not supported by any of the four routes above, nor by the mapped envelope of Li (2026), whose area is 48.2 per cent west-facing and 33.8 per cent north-west-facing. The source lies on the north side of the massif on a slope that faces west. Both statements hold simultaneously.

2.3 Matched control discs

Each measurement on the source is referred to 120 control discs of the same radius drawn elsewhere in the same scene. Discs are drawn at random subject to lying at least 2 km from the source, containing at least 1,500 valid pixels, and matching the source on median local incidence angle within the range 56 to 70°, on circular-mean aspect within 35°, and on median slope within 10°. The draw is deterministic under a fixed seed. Matched medians are 59.6° local incidence, 274.9° aspect and 32.1° slope, against source values of 62.3°, 272.8° and 33.4° (Figure 2).

The controls answer the question of whether the source behaved differently from comparable slopes that did not fail. They are the operative null for the amplitude and displacement tests. For coherence, Section 4 shows that the source's own history is the stronger null and explains why.

2.4 Placement of the source disc

The analysis disc is a 500 m circle centred on 28.2853 °N, 85.5252 °E. Two independent reconstructions place the source elsewhere: the rapid hazard assessment at 28.288708 °N, 85.528159 °E, 477 m to the north-north-east, and Li (2026) at a preferred centroid of 28.28858 °N, 85.52701 °E, 405 m in the same direction. The two agree with each other to within about 90 m and disagree with the centre used here. Li additionally maps the changed source surface as 1.009 km^2 with a maximum planimetric dimension of 1,151 m, so the failure is larger than a 1 km disc can cover.

Two questions follow, and they have different answers.

Is the disc sampling the right terrain? Li's independently mapped preferred envelope gives a median elevation of 4,991 m, a median slope of 34.8°, and a circular mean aspect of 280.8°, with 48.2 per cent of its area west-facing and 33.8 per cent north-west-facing. The disc used here gives 5,000 m, 33° and 273°. Those are close agreement on terrain from an entirely separate mapping exercise, so the disc is sampling the failure's terrain even though its centre differs.

Is it sampling where the surface actually changed? This can be tested rather than argued, because the interval containing the collapse provides ground truth: a disc overlapping the detachment must decorrelate. Repeating the coherence analysis with the disc centred on each candidate gives:

	28.2853, 85.5252	28.288708, 85.528159
usable pixels	3,945	5,916
median local incidence	62.3°	52.8°
median slope	33°	21°
shadow	24.6%	9.8%
five quiet intervals	5.1 ± 2.8%	12.5 ± 4.8%
interval containing the failure	18.0%, z = +4.57	13.0%, z = +0.10
interval ending 50.6 h before	z = +0.06	z = +1.39
2 s.d. bound	10.8%	22.1%

The disc centred on the alternative coordinate shows no coherence signature of the collapse whatever: 13.0 per cent against a quiet mean of 12.5, a departure of one tenth of a standard deviation. The disc used here shows the same event at 4.57 standard deviations. A disc registering nothing cannot be sampling the part of the surface that changed, and the placement adopted here is therefore supported by the event itself rather than by any external coordinate.

The reason is instructive and generalises. The alternative disc lies on gentler ground — 21° rather than 33°, 53° local incidence rather than 62°, a tenth of the shadow — and yields 50 per cent more usable pixels. By every conventional measure it is the better-observed target. But its quiet baseline sits at 12.5 per cent of the disc below coherence 0.15, against 5.1 per cent for the disc adopted, so it begins much closer to the decorrelation floor and has little dynamic range in which an event can express itself. More usable pixels does not mean more detection power, and a target selected on observability alone can be the wrong target.

Two limits follow and are carried through the rest of the paper. The bounds reported here apply to the portion of the failure this disc samples, not to the whole detachment, whose mapped extent exceeds the disc diameter. And the bounds are specific to this location: at the alternative centre the same method would have returned a limit of 22.1 per cent of the usable disc, more than twice as weak.

2.5 What the area of interest does and does not cover

The area of interest is a source-area analysis, not a flood-extent one. Both candidate detachment coordinates lie inside it. The Rasuwagadhi border crossing lies 6.1 km beyond its western edge, Kyanjin Gompa 1.3 km south, and Syafrubesi 12.5 km out. Only 2.12 per cent of the area lies below 3,000 m, all of it in the north-west corner, so the runout terminus and the barrier lake reported at the valley floor sit at the boundary rather than within it. No inference about the flood path, the barrier lake or downstream impacts is drawn here; mapped extent for this event is available from Copernicus Emergency Management Service activation EMSR927, "Flood in Nepal", activated 26 August 2026 at 09:53 UTC at the request of DG ECHO and covering six areas of interest, and from UNOSAT, whose mudflow and rockflow impact assessment for Rasuwa and Nuwakot districts as of 26–27 August delineates a 37.353 km^2 disturbed footprint. UNOSAT separately mapped newly formed barrier lakes in Rasuwa district as of 28 August, which is the authoritative source on the impoundments referred to in Section 6 and the reason no inference about them is drawn from the area of interest used here.

It is worth recording that the Copernicus activation was requested on the initial understanding that the flood had been triggered by a glacial lake outburst. That attribution did not survive subsequent analysis, and the sequence is now described as a rock and ice failure at high elevation. Rapid-mapping products are produced under time pressure from the information available at activation, and their event attribution should be read accordingly; their mapped extents remain the best available.

---

3. Amplitude

3.1 Track B, 50.6 hours before failure

Median co-polarised backscatter change on the source disc over 12 to 24 August is **+0.14 dB**, at the **67.5th percentile** of the 120 matched controls. Controls were matched on incidence, aspect, slope and elevation, with matched medians of 59.4°, 272°, 32° and 4,865 m against source values of 61.8°, 270°, 32° and 5,034 m.

Over the following interval, 24 August to 5 September, which contains the failure, the same measurement gives **−2.96 dB**, below all 120 controls without exception.

The contrast between those two numbers is the calibration. A test that returns nothing before the event and nothing after it would be uninformative. This test returns an unambiguous detection after the event and a value inside the ordinary range of non-failing slopes before it.

3.2 Track A, and the effect of the geometry filter

Track A views the same face far less favourably: median local incidence 82.1° against 71.0°, with 50.4 per cent of the disc in shadow against 24.6 per cent, leaving only 14.4 per cent usable against 44.3 per cent. Scene-wide the two tracks are more similar, 67.5 against 82.2 per cent usable, so the disparity is specific to this steep west-facing slope rather than a property of the frame.

Applying the same incidence and shadow filter used on track B, and intersecting validity across the three track A dates, leaves 903 pixels — fewer than the 14.4 per cent of the disc that the geometric filter alone retains, because pixels must also return valid backscatter on all three dates — at median incidence 64.8°, slope 27° and aspect 269° — geometry comparable to track B on roughly a quarter of the sample.

interval	shadow mask only	incidence-filtered	vs 120 controls
7 → 19 Aug, VV	+0.29 dB	+0.54 dB	91.7th percentile
19 → 31 Aug, VV	−3.63 dB	−5.56 dB	below all 120
7 → 19 Aug, VH	+0.32 dB	+0.56 dB	
19 → 31 Aug, VH	−2.08 dB	−3.54 dB	

The filter improves sensitivity rather than merely reducing sample size. The post-event drop deepens from −3.63 to −5.56 dB in the co-polarised channel and from −2.08 to −3.54 dB in the cross-polarised channel, because the unfiltered mask dilutes the measurement with near-grazing pixels sitting close to the noise floor, which have limited room to fall. This is a measurable demonstration that geometry selection, rather than pixel count, governs detection capability on steep terrain.

The pre-event track A interval reaches the 91.7th percentile of its matched controls, the highest pre-event value in either track. It should not be read as a hint of precursory change, for three reasons. It is a rise, whereas the failure mechanism produces a fall. The interval ends 171 hours before failure rather than 50.6. And the control match is materially poorer than on track B — matched medians of 60.7° incidence and 22° slope against source values of 64.8° and 27°, where track B achieved 59.4° against 61.8° and 32° against 32° — because the usable set under track A geometry is small and biased toward gentler ground, so the null itself is weaker.

The two tracks are therefore not equivalent observations of the same slope. One sees 44 per cent of the disc at 71°, the other 14 per cent at 82°. Track A corroborates track B, and does so more strongly on the post-event side, but its pre-event interval carries the caveats above. The same disjunction appears in the one prior study of coherence before a slope failure: Jacquemart and Tiampo (2021) report that the ascending track gave the more reliable coherence ratios at Mud Creek even though it was the geometry less suited to measuring that slope's precursory deformation. The track that best measures a slope and the track that best detects change on it need not be the same track.

---

4. Coherence

4.1 Why the disc-median statistic was discarded

Coherence loss is a standard basis for detecting slope failures from radar, and the choice among candidate coherence statistics has itself been examined: Burrows et al. (2020) test five coherence-based detection methods against four triggering earthquakes on two sensors and find that which performs best depends on the sensor, although their concern is mapping failures after they occur rather than before; and Jacquemart and Tiampo (2021) use time series of coherence to characterise pre-failure activity at the Mud Creek landslide in California, which is the closest published precedent for the design used here and is returned to in Section 6.2. That choice is consequential here, because two statistics computed from the same interferograms give opposite answers on this target. The natural first statistic is median interferometric coherence on the source disc. It fails on this target, and the failure is instructive rather than incidental.

Median coherence over 12 to 24 August places the source at the 17th percentile of the matched controls. Median coherence over 12 August to 5 September — an interval containing the detachment of a mass large enough to register at M5.2 — places it at the 13th percentile. The interval containing the collapse is statistically indistinguishable from the interval before it.

The reason is that the source begins near the decorrelation floor. Its median coherence falls from 0.514 in late June to 0.333 by late August, so a level statistic has little room left in which an event can express itself. An early reading of the small percentile difference as a weak precursory hint was withdrawn on this basis. A statistic that cannot distinguish a catastrophic failure from a quiet fortnight cannot be used to exclude a precursor.

4.2 The threshold fraction

The statistic used instead is the fraction of the usable disc falling below a coherence of 0.15 — a shape rather than a level, and sensitive to localised decorrelation on a target whose overall coherence is already low. The same reasoning has been applied elsewhere: Dini et al. (2026) track patterns of coherence loss over confined areas as a proxy for localised strain, and identify structures along the eventual scarp of the Achoma landslide in Peru five years before it failed.

interval	median coherence	fraction below 0.15	largest connected patch
25 Jun – 07 Jul	0.514	4.1%	0.47 ha

interval	median coherence	fraction below 0.15	largest connected patch
07 – 19 Jul	0.599	6.2%	1.04 ha
19 – 31 Jul	0.714	1.1%	0.30 ha
31 Jul – 12 Aug	0.492	8.8%	1.93 ha
12 – 24 Aug	0.333	**5.3%**	0.69 ha
12 Aug – 05 Sep (spans failure)	0.270	**18.0%**	2.57 ha

The five pre-event intervals give 5.1 ± 2.8 per cent, ranging from 1.1 to 8.8 (Figure 1). The interval containing the failure gives 18.0 per cent, a departure of **z = 4.57**. The interval ending 50.6 hours before failure gives 5.3 per cent, **z = +0.06** — the median of its own distribution, ranking third of five.

4.3 The detection bound

Taking the quiet mean plus two standard deviations gives 10.7 per cent of the usable disc, approximately 4.2 ha in total area, and no quiet interval contains a connected low-coherence patch exceeding 1.93 ha. The bound is therefore:

> No surface disturbance above approximately 2 ha of coherent decorrelation occurred on the source face in the twelve days ending 50.6 hours before failure.

For scale, the usable disc on which this is measured covers 39.5 ha, and the mapped detachment discussed in Section 2.1 covers roughly 100 ha. The bound therefore corresponds to about five per cent of the area sampled, and about two per cent of the area that eventually failed.

This bound rests on the temporal null, not the spatial one, for reasons set out in Section 6.2. It is also specific to this disc placement; at the alternative coordinate examined in Section 2.4 the same method would return 22.1 per cent, more than twice as weak.

---

5. Line-of-sight displacement

5.1 The single-pair noise floor

Unwrapped phase converts to line-of-sight displacement at 4.413 mm per radian for the 5.546 cm wavelength, one fringe corresponding to 27.7 mm. Displacement was measured on the 12 to 24 August pair over the same 120 control discs, restricted to pixels with coherence above 0.3 in that pair.

Control scatter is **6.13 mm** at one standard deviation (Figure 3). It correlates with disc median elevation at **r = −0.72**, which is stratified tropospheric delay across 2.4 km of relief. The source lies 2.84 mm below the control median, at the **37th percentile** — not a detection.

Absolute values are arbitrary: no atmospheric correction is applied and no reference point is chosen, so only relative positions within the control distribution carry meaning.

5.2 Projection geometry

Comparing a reported downslope rate to a line-of-sight measurement requires the projection factor, which is derived here from the measured geometry rather than assumed. Solving for the radar look angle that reproduces the measured local incidence angle of 62.3° on a slope of 33.4° at aspect 272.8° gives **29.2° from vertical**, at the near-range edge of the Sentinel-1 interferometric wide swath. That the solution falls inside the instrument's physical range is an independent check on the geometry chain.

On that geometry, downslope motion projects onto the line of sight with a factor of **0.881**, stable between 0.876 and 0.884 across any plausible satellite azimuth, and with negative sign: the source moves away from the sensor. The reported rate of 10 mm per month therefore implies about 3.5 mm of line-of-sight displacement per twelve-day pass, against the 6.13 mm noise floor of Section 5.1.

5.3 Cumulative displacement over sixty days

Five consecutive twelve-day pairs from 25 June to 24 August were chained. For each interval the median displacement on each disc was detrended against disc median elevation, removing the stratified tropospheric term; residuals were then summed per disc across the five intervals.

A prediction was recorded before the test was run. Since the reported rate *reached* 10 mm per month by mid-August, the mean over this window must be lower, giving an expected cumulative displacement of −17.4 mm at the peak rate to −10.4 mm at 60 per cent of it, negative in sign.

interval	residual s.d.	r with elevation	source residual
25 Jun – 07 Jul	**15.07 mm**	**+0.07**	**−13.87 mm**
07 – 19 Jul	4.75	−0.63	+4.65
19 – 31 Jul	3.76	+0.55	+3.33
31 Jul – 12 Aug	2.17	+0.93	+0.06
12 – 24 Aug	4.22	−0.71	−1.06

Values for the 12–24 August interval differ slightly from those in Section 5.1 because the mask differs: Section 5.1 requires validity across the six coherence products, whereas the chain additionally requires validity in all five phase products, which removes further pixels. Raw scatter for that interval is 6.01 mm against the 6.13 mm of Section 5.1, and the elevation correlation −0.71 against −0.72. The detrended residual of 4.22 mm is a different quantity again, being the scatter that remains after the elevation term is removed.

Residual scatter follows $\sigma\sqrt{(1-r^2)}$ closely, which is why the first interval is uninformative: with r = 0.07 the detrend removes essentially nothing, and whatever inflates that interferogram to 15 mm is not elevation-dependent — turbulent atmospheric delay, or unwrapping difficulty at monsoon onset.

Over the full sixty days the source lies 9.07 mm below the control median, of the predicted sign and just under the predicted magnitude, but the control scatter is 16.49 mm, giving **z = −0.55** at the 31st percentile. The measured chained scatter exceeds the 13.40 mm that independent intervals would produce, because atmospheric delay does not average down as white noise does.

That apparent agreement does not survive inspection, since the anomalous first interval supplies 13.87 mm of the 9.07 mm cumulative. Excluding it, the remaining forty-eight days give a tighter control scatter of 8.93 mm but place the source at **+7.31 mm, z = +0.82** — the opposite sign to the prediction. The two results must be reported together; either alone would mislead.

An unwrapping screen flagged 4 disc-intervals of 599 as lying within 4 mm of a fringe multiple beyond half a fringe; the source was clean in all five intervals, so the chain is not corrupted by fringe jumps.

5.4 The displacement bound

Twice the control scatter, divided by the projection factor and scaled to a month, gives **19.0 mm per month over sixty days** and **12.8 mm per month over forty-eight**. Both lie above the rate reported from the multi-month stack. This analysis therefore neither confirms nor excludes that rate, and the bound is a statement about what could have been ruled out, not about how fast the slope moved.

---

6. Discussion

6.1 What the three measurements bound

Taken together the amplitude, coherence and phase tests place quantitative limits on what the last pre-failure acquisition contained. Amplitude change on the source disc sat at the 67.5th percentile of 120 geometry-matched controls, well inside the range of slopes that did not fail. The fraction of the usable disc below coherence 0.15 was 5.3 per cent, ranking third of the five quiet intervals and 0.06 standard deviations from their mean; the same statistic reaches 18.0 per cent, z = 4.57, once the failure is inside the interval. Line-of-sight displacement from the same pair placed the source 2.84 mm below the control median, at the 37th percentile, against a control scatter of 6.13 mm.

None of these is a null in the weak sense of a test that was underpowered against everything. The post-event amplitude change of -2.96 dB falls below all 120 controls, and the co-event coherence anomaly is a four-and-a-half sigma departure from the source's own history. The instruments and the statistics detect this event decisively once it has happened. What they do not do is see it coming.

The bound is therefore worth stating as a positive result rather than an absence. Taking the quiet mean plus two standard deviations, a disturbance affecting more than 10.7 per cent of the usable disc would have exceeded normal variation, and no quiet interval contains a connected low-coherence patch larger than 1.93 ha. No surface disturbance above approximately 2 ha of coherent decorrelation occurred on the source face in the twelve days ending 50.6 hours before failure.

6.2 The temporal null is stronger than the spatial one

A methodological point falls out of the coherence result and is likely to transfer to other targets. Against the 120 matched control discs, the interval containing the collapse reaches only the 92nd percentile on the threshold fraction — a weak separation. Against the source's own five quiet intervals the same statistic gives $z = 4.57$.

The reason is that the source disc has idiosyncratic character that spatial matching cannot remove. It sits at near-grazing incidence on a glaciated surface; matching on median incidence, circular-mean aspect and median slope brings the controls close in geometry but not in scattering behaviour. The source's own history controls for that exactly. The closest prior use of coherence as a pre-failure indicator resolves the same tension by a different route. Jacquemart and Tiampo (2021) track the ratio of mean coherence on the unstable slope to that of the surrounding hillslope, and report that ratio falling by half as the Mud Creek landslide began to accelerate five months before its catastrophic failure, with comparable behaviour during an earlier acceleration a year before. That design is neither purely spatial nor purely temporal: the ratio removes scene-wide effects epoch by epoch, and the time series then supplies the baseline against which a change is judged. What is used here is the temporal half of the same idea, applied on a target where the spatial half has little to work with, since a near-grazing glaciated face has no close counterpart among the matched neighbours. The difference in outcome is worth stating alongside the difference in method. A statistic of this class fell by half five months ahead of failure at Mud Creek; here the equivalent statistic gives $z = +0.06$ fifty hours ahead of failure. The null reported here is a null from a method with demonstrated sensitivity elsewhere, not from an untested one. Dini et al. (2026) extend that approach at the Achoma landslide, where the same coherence ratio held near unity for five years and fell below 0.8 only three months before failure, and they state the condition under which such methods should be expected to work: on larger, slower or more complex landslides where deformation evolves progressively, rather than on rapid failures that occur with little measurable precursory motion. That criterion was set out independently of this event, and whether this slope meets it is precisely what these products cannot settle. The rate reported from the multi-month stack suggests a progressive process, but the failure surface lay beneath the ice, so the deformation the criterion asks about is not what a C-band sensor was observing here. This also explains why the disc-median statistic failed while the threshold fraction succeeded: a median is a level, and levels are dominated by the idiosyncrasy, whereas the fraction below a threshold is a shape.

The practical consequence is that spatial controls belong in the amplitude test and in demonstrating that the geometry matching is real, but the detection bound must rest on the temporal null.

6.3 Why a single pair cannot reach the reported rate

Two independent claims of pre-failure motion exist and they are not the same claim. Movement of roughly 10 mm per month near the collapse area, from an eight-month Sentinel-1 stack spanning 8 January to 18 August 2026, has been reported by Shirzaei (in Basu, 2026); the analysis is not peer reviewed, no time series has been published, it is described by its author as preliminary, and the stated acceleration extends into the final week, which lies outside the observation window.

It should be stated plainly that the position taken in that interview is close to the one reached here, and that the bound reported below is not offered as a rebuttal. Shirzaei describes the event as difficult to anticipate, notes that many glaciers and rock slopes move continuously without collapsing, states that the timing of collapse was hard to forecast, and is explicit that the acceleration alone would not have indicated an imminent collapse — its value would have been to flag the area as a hotspot warranting closer monitoring. That is a screening claim, not a warning claim, and it is compatible with everything reported here. Separately, Guo et al. (2026) report Sentinel-2 feature tracking over 2024 to 2026 showing that the middle and lower parts of the source glacier maintained relatively high surface velocities throughout, with the detachment situated at the upper margin of the fast-flowing zone where the velocity gradient concentrates extensional and shear deformation. That is a description of a multi-year state, not of a pre-failure acceleration, and it is measured by optical feature tracking rather than interferometry. The bound reported here speaks to neither directly: it constrains what a routine interferometric product could have resolved over the two months before failure.

Solving for the radar look angle that reproduces the measured local incidence angle of 62.3 degrees on a slope of 33.4 degrees at aspect 272.8 degrees gives 29.2 degrees from vertical, at the near-range edge of the Sentinel-1 IW swath — an independent consistency check on the geometry. On that geometry, downslope motion projects onto the line of sight with a factor of 0.88, stable across any plausible satellite azimuth, and with negative sign: the source moves away from the sensor. The reported rate therefore implies about 3.5 mm of line-of-sight displacement per twelve-day pass, against a measured single-pair noise floor of 6.13 mm. The signal is inside the noise, and the dominant term in that noise is tropospheric: it correlates with disc median elevation at $r = -0.72$ over 2.4 km of relief.

Chaining does not rescue it, for the reasons set out in Section 5.3: atmospheric delay does not average down as white noise does, so the chained control scatter over sixty days exceeds what independent intervals would give, and the one interval that appears to support the predicted sign is also the one whose noise cannot be detrended.

The bounds these place on line-of-sight motion are 19.0 mm per month over sixty days and 12.8 mm per month over forty-eight. Both lie above the reported rate. This analysis therefore cannot confirm or exclude it, and that is the finding: routine twelve-day products, singly or chained over two months, do not reach the precision at which the reported deformation was measured.

6.4 Detection is not warning

The distinction the preceding sections force is between detecting anomalous behaviour and issuing a warning, and it is not a matter of degree.

A physical constraint compounds the sampling one. The consensus that has emerged from post-event imagery is that bedrock beneath the ice failed and carried the overlying glacier with it, the ice being a passenger rather than the trigger. If the failure surface lay beneath the glacier, then a C-band sensor observing the ice surface was not observing the surface where the process was developing. The absence of a signature in these products is therefore expected on physical grounds as well as on grounds of precision and revisit interval, and Cook's observation that no current technique detects subglacial landslides automatically follows directly.

The reported rate is three orders of magnitude below typical glacier flow of tens to hundreds of metres per year. Whatever was measured is therefore not glacier motion but creep in the rock and frozen debris beneath it, which is consistent with a bedrock detachment carrying ice above it rather than a failure within the ice. Motion at that rate is measurable from orbit — but only by a multi-epoch inversion that estimates the atmospheric contribution from the stack itself. The data required were free, already in the archive, and available to anyone. The limitation was not the sensor.

Warning is a different problem. Slopes of this kind commonly accelerate over hours to days before failure, and forecasting methods that extrapolate inverse velocity to a failure time need sampling at that cadence. Faillettaz et al. (2015) review the rupture mechanisms behind such instabilities and the early-warning perspectives that follow from them, classifying them by the thermal regime at the ice–bedrock interface and the presence of liquid water — the same interface implicated below. Sentinel-1 revisits this latitude every twelve days, or six with both satellites in the constellation. The entire terminal phase of such an acceleration falls inside a single revisit interval. The present results are the direct demonstration: at the last pre-failure acquisition, 50.6 hours before the event, amplitude, coherence and phase each show nothing distinguishable from the source's own quiet behaviour or from 120 matched neighbouring slopes.

A precedent exists for the interval available, and it is instructive about the distances involved. At Chamoli, where a rock and ice avalanche caused the February 2021 disaster (Shugar et al., 2021), Tiwari et al. (2022) recorded continuous high-frequency tremors in the 10 to 35 Hz band for approximately 2.5 hours before the main detachment, with tremor amplitude rising and the interval between successive tremors shortening as failure approached. Cross-correlation located these signals at the source of the failed wedge, and weaker precursors were identifiable a day earlier. Critically for the design of any monitoring network, those high-frequency precursors were recorded only at the nearest station, 12 km from the source, with a portion weakly detected at the next station; the main detachment itself, at 1 to 5 Hz, registered across the entire Himalayan network. High-frequency energy from crack propagation attenuates rapidly, so the signals that would warn do not travel, while the signal that travels is the failure. Roughly 15 to 17 minutes elapsed between the avalanche release and the destruction at the Tapovan hydropower station, which those authors argue would have been sufficient for evacuation had a local system been in place. The corresponding interval here is seven minutes to the border post. Guo et al. (2026) report candidate seismic signals at a regional broadband station within approximately three hours of this failure. Neither set of signals has been shown to be identifiable in advance without knowledge of the event, but the timescale at which the relevant activity occurs is consistent across the two cases, and it is a timescale no satellite in a twelve-day orbit can sample.

The same gap is identified from the other direction by Shirzaei, who observes that most existing systems address glacial-lake outburst floods rather than glacier–rock collapses, that operational examples exist — real-time monitoring of lake level, ice and rock collapses and downstream runoff at Cirenmaco in Tibet, and water-level sensors, weather stations and sirens in the Khumbu — and that what is largely missing is a regional satellite-based system routinely searching for accelerating glacier and rock-slope deformation and connecting it to downstream flood and avalanche modelling. The measurements reported here quantify the precision such a system would need to exceed if it were built on routine twelve-day products.

Field evidence of permafrost-related slope failure exists in this valley specifically. Baral et al. (2023) document thaw slumps on the route to Yala Glacier and permafrost slope failures near Kyanjin village, both in the Langtang, in a review that finds consistent regional warming and increasing landslide activity across High Mountain Asia while noting that direct permafrost observation in the Hindu Kush Himalaya remains limited to a handful of monitoring sites.

Closing that gap requires instruments with minute-to-hour sampling — ground-based radar, GNSS on the moving mass, extensometers, or a local seismic array — installed on the slope in question. On a glaciated face above 5,000 m that is a substantial undertaking, and there are thousands of comparable slopes across High Mountain Asia. Neither approach substitutes for the other: satellite observation can identify which slopes merit instruments, and instruments can produce warnings, but satellite observation alone cannot.

6.5 Relation to the Chamoli precedent

The closest published analogue to this study is Van Wyk de Vries et al. (2022), who examined the February 2021 Chamoli rock–ice avalanche using three decades of optical imagery, feature tracking, repeat digital elevation models and Sentinel-1 interferometry. Their conclusions on the interferometric component are unambiguous and closely mirror what is found here on a different slope. Of 108 twelve-day interferograms spanning January 2017 to November 2020, roughly half lost coherence entirely; coherence was retained only on the ice-free lower part of the failed block, with the glacier-covered upper part decorrelated throughout. They conclude that Sentinel-1 interferometry would not have provided an adequate monitoring tool in that case even with prior knowledge of the location of the instability.

They also identify the same geometric mechanism reported in Section 3.2 of this paper. The north-facing aspect of the Chamoli source presented a twofold difficulty: illumination was limited, giving low backscatter, and downslope motion was oriented close to the direction in which the sensor is least sensitive. The present analysis quantifies both effects on a west-facing slope viewed from a descending pass, where the projection factor is favourable at 0.881 but the incidence angle on one of the two available tracks reaches 82 degrees.

Two differences define the contribution made here. Their assessment of the interferometric record is qualitative: coherence was lost, fringes could not be identified, and the method is judged inadequate. No bound is stated. This paper reports what could and could not have been resolved as measured quantities — a disturbance of approximately 2 ha, a displacement of approximately 13 mm per month — which allows the limit to be compared directly against a reported deformation rate rather than asserted. And their study proceeds throughout with knowledge of the failure location, which they state explicitly; the matched-control design used here tests whether the source would have been distinguishable without it.

Their broader conclusion, that precursory signs at Chamoli were identifiable retrospectively while the timing of collapse could not have been forecast from satellite data alone, is consistent with the position reached here.

6.6 The pre-event indications reported elsewhere

The rapid hazard assessment prepared for this event reports three pre-event indications: an ice surface speeding up toward the eventual failure location shortly before the collapse, meltwater visibly discoloured by 24 August, and some sign of a crack propagating into the surrounding bedrock slope in the days beforehand. These are not in conflict with the limits reported here, and the reasons are worth stating precisely, because a reader encountering both may take them to be.

The assessment presents these observations explicitly in hindsight and hedges each of them. It does not claim they were identified in advance, and no operational monitoring was drawing on them at the time.

The observations also come from a different class of sensor. That assessment drew on Landsat 9 and Planet imagery; the present analysis uses Sentinel-1 products at 40 m. A crack propagating through a bedrock slope is a linear feature metres in width. It is resolvable in metre-scale commercial optical imagery and cannot be resolved at 40 m under any circumstances, so its existence places no constraint on a decorrelation bound expressed in hectares. Discoloured meltwater is likewise an optical observation with no radar equivalent: backscatter at C band responds to surface roughness and dielectric properties, not to suspended sediment colour.

The third indication, acceleration of the ice surface, is the one that overlaps with what is measured here, and Section 6.3 gives the quantitative answer: at the rate independently reported for this slope, the expected line-of-sight displacement is below the single-pair noise floor and below the bound obtainable by chaining five consecutive pairs.

Two distinctions therefore separate the two sets of results, and neither is a disagreement. One is retrospective and one is prospective. One uses commercial metre-scale optical imagery, tasked and interpreted after a known failure; the other uses free 40 m radar products of the kind a standing monitoring service would hold. The observations reported elsewhere are real. They were not available, at that resolution or in that form, to anyone watching this valley before 26 August.

6.7 What distinguished the year that failed

Sections 3 to 5 establish that none of the three pre-failure measurements made here separates the source from comparable slopes. Four further quantities, drawn from outside this analysis, likewise fail to separate 2026 from years in which nothing failed.

The spring-minus-winter polarisation contrast reported in the Supplementary Material is matched by 2019 to within 0.01 dB, −2.61 against −2.62, and 2019 also had the earliest melt trough in the ten-year record, at day 114 against day 113; no failure followed it. The ten-year amplitude climatology on the same relative orbit places 2026 at the median across the late-season window. Antecedent precipitation from reanalysis was lower in 2026 than in 2019 at three, seven and fourteen days — 37 against 80 mm, 95 against 140, and 249 against 272 — with dry conditions for roughly five hours before failure; Li (2026) reach the same conclusion independently, from prespecified windows and two products, finding that neither GPM IMERG nor ERA5-Land places any of five antecedent windows in an unusually wet upper tail, and that the IMERG 7, 14 and 30-day totals fall below all twenty-five matched years since 2001. And no tectonic seismicity occurred in the thirty days beforehand: both entries in the catalogue for that window are classified as landslides, so a seismic trigger is excluded down to the catalogue's completeness limit of magnitude 4 to 4.5.

A spatial null points the same way. Among the thirteen sites of the spring climatology, the slope that failed was not the most extreme in 2026, ranking second; one control site was more anomalous and is still standing.

One quantity does separate 2026, and it is not one measured here. Li (2026) report that the seven-day mean air temperature at two metres above ground, and the seven-day positive-degree-day total — a temperature-index proxy for melt rather than a measurement of it — both ranked above all twenty-five matched years, with a five-day warm spell ending on 25 August. Thermal preconditioning is therefore the candidate that survives when the others are excluded, and it is precisely the quantity no orbital sensor measures at the failure surface. Field evidence of permafrost-related slope failure exists in this valley (Baral et al., 2023), and the mechanism is consistent with the post-Little-Ice-Age debuttressing discussed in Section 6.4. Permafrost is not spatially observable in the way glaciers are, lying beneath the active layer and so largely outside the reach of satellite remote sensing; across the Hindu Kush Himalaya its presence and changes are inferred rather than measured, from evidence gathered mostly in other permafrost regions, even though permafrost area exceeds glacier area in nearly every country of the region (Gruber et al., 2017). The thermal state of a failure surface at this elevation is therefore not a quantity any dataset supplies, orbital or otherwise.

A caveat belongs with that statement. The absence of a detectable signature is a statement about these measurements at these precisions, and the preceding section establishes that at least one quantity — slow deformation — was in fact present and measurable by a method not applied here. The claim is not that nothing was happening. It is that nothing was visible in the products a monitoring service would have been using.

6.8 What a multi-epoch inversion would have to beat

The bounds reported here define the precision a stacked analysis must exceed to be useful for screening rather than for post-event attribution. A multi-epoch inversion over this frame, using the redundancy of a dense interferogram network to estimate and remove the per-date atmospheric term, would reach a few millimetres per year where the products examined here reach approximately 13 mm per month. Such an inversion across the pre-failure period on this frame remains to be published.

7. Conclusion

Backscatter amplitude, interferometric coherence and single-pair line-of-sight displacement on the source face 50.6 hours before failure were each indistinguishable from the same slope's quiet behaviour and from 120 geometry-matched neighbouring slopes. The same statistics identify the collapse decisively once it falls inside the observation interval, so these are calibrated limits rather than uninformative nulls: no surface disturbance above approximately 2 ha of coherent decorrelation occurred in the twelve days ending 50.6 hours before failure, and no line-of-sight displacement above approximately 13 mm per month occurred over the preceding seven weeks.

That second bound lies above the rate subsequently reported from a multi-month stack, which is the substantive point. The deformation was measurable from orbit, using data that was free and already archived, but not by the twelve-day products a monitoring service would have been screening. Detection at these rates requires a multi-epoch inversion with atmospheric correction estimated from the stack; warning requires sampling at the hours-to-days cadence over which such slopes accelerate. No freely available constellation provides that at this latitude. Commercial high-resolution radar can be tasked at shorter intervals, but tasking presupposes a slope already identified as of concern, which returns the problem to screening.

The interval available even to a perfect detector is short. The seismic signature of the failure is timed at 08:37 local, and the flood wave reached the border post at Rasuwagadhi at about 08:44 – seven minutes. The rapid hazard assessment for this event records that no operational early warning system for glacier-related hazards existed at this location, that warning time from conventional in-channel systems would have been minimal and probably insufficient for evacuation at the border post, and that further downstream, warning times of ten minutes or more from capable systems could have saved a significant number of lives. It also notes that the mass movement produced a seismic signal above magnitude 4, and that seismic networks may therefore support early warning over large areas.

That is the shape of the problem. Upstream, no amount of orbital precision converts into usable warning time, because the process is subglacial, the revisit interval is twelve days and the terminal phase is minutes long. Downstream, where warning times run to tens of minutes, the constraint is not detection at all but whether a system exists to carry the signal and act on it. The limitation identified here is neither the sensor nor the data policy, but the gap between what routine products resolve and what a forecast would need – and, below the source, the gap between a signal being generated and anyone being in a position to use it.

Figure captions

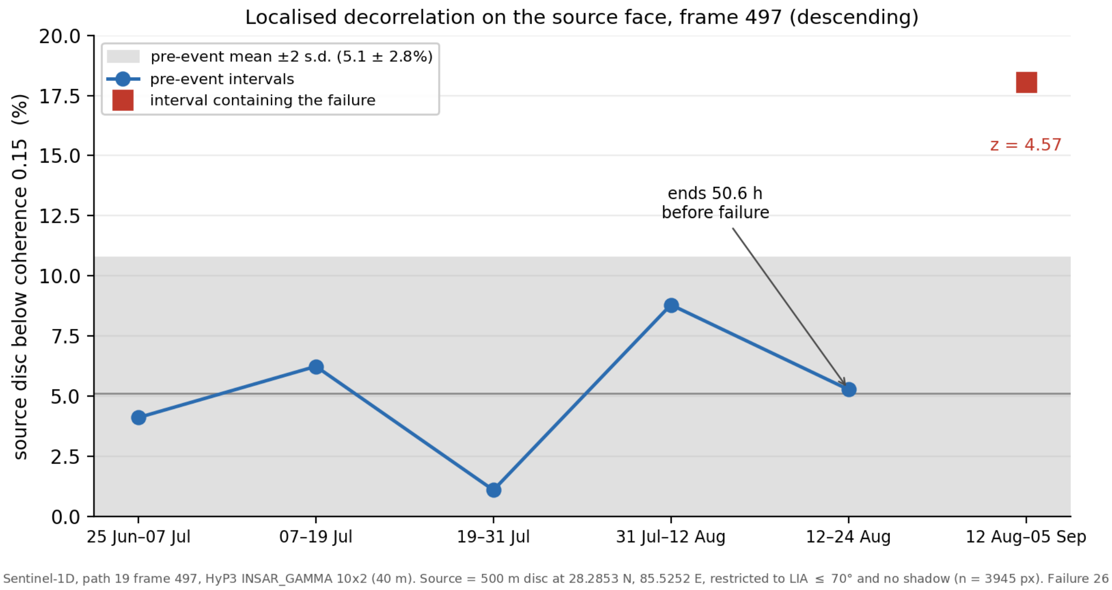

Figure 1. Localised decorrelation on the source face, track B. Fraction of the usable source disc falling below coherence 0.15, for five consecutive twelve-day intervals and for the 24-day interval spanning the failure. Shaded band is the pre-event mean ± 2 s.d. (5.1 ± 2.8 per cent). The interval ending 50.6 hours before failure ranks third of five; the interval containing the failure departs by z = 4.57. Sentinel-1D, path 19 frame 497, HyP3 INSAR_GAMMA at 10 × 2 looks (40 m). Source disc of 500 m radius at 28.2853 °N, 85.5252 °E, restricted to local incidence ≤ 70° and no shadow, n = 3,945 pixels.

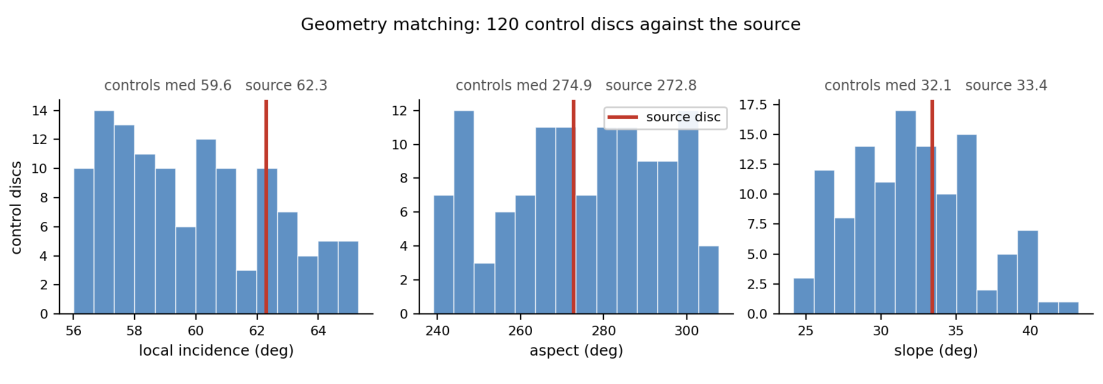

Figure 2. Geometry matching of the 120 control discs. Distributions of median local incidence angle, circular-mean aspect and median slope across the control discs, with the

source disc marked. Matched medians are 59.6°, 274.9° and 32.1° against source values of 62.3°, 272.8° and 33.4°. Discs of 500 m radius, at least 2 km from the source, drawn at random subject to matching on local incidence (56–70°), aspect (± 35°) and slope (± 10°). Slope and aspect from the Copernicus GLO-30 model supplied with the interferometric products.

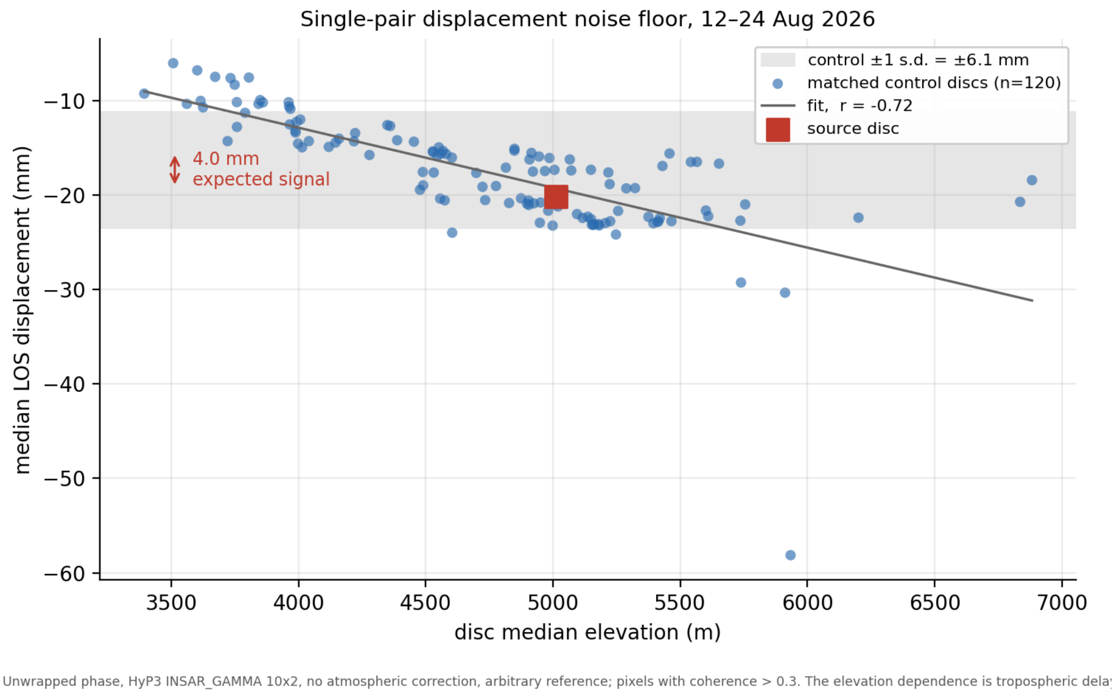

Figure 3. Single-pair displacement noise floor, 12–24 August 2026. Median line-of-sight displacement on each of the 120 matched control discs against disc median elevation, with the source disc marked. Shaded band is ± 1 s.d. of the controls (6.13 mm); the fitted line gives r = −0.72, which is stratified tropospheric delay across 2.4 km of relief. The arrow shows 4.0 mm, the displacement expected from the reported rate of 10 mm per month over twelve days before projection onto the line of sight; applying the 0.881 factor derived in Section 5.2 gives 3.5 mm. Either value lies inside the control band. Unwrapped phase from HyP3 INSAR_GAMMA, pixels with coherence above 0.3, no atmospheric correction and an arbitrary reference, so only relative positions carry meaning.

Data and code availability

Sentinel-1 products are freely available from the Copernicus Data Space Ecosystem and the Alaska Satellite Facility. Analysis code and derived data are archived at Zenodo, doi:10.5281/zenodo.22676918 (version 2.0.0); version 1.0.0 of that record, doi:10.5281/zenodo.22541072, holds the material for the companion amplitude study. Contains modified Copernicus Sentinel data 2017–2026.

References

Baral, P., Allen, S., Steiner, J. F., Gurung, T. R. and McDowell, G. (2023) Climate change impacts and adaptation to permafrost change in High Mountain Asia: a comprehensive review. *Environmental Research Letters*, 18(9), 093005. doi:10.1088/1748-9326/acf1b4

Basu, M. (2026) Satellite images before Nepal disaster showed warning signs. *Nature*, 657, 328–329. doi:10.1038/d41586-026-02746-4 [News Q&A interview with M. Shirzaei, 2 September 2026; the analysis discussed is preliminary and not peer reviewed]

Burrows, K., Walters, R. J., Milledge, D. and Densmore, A. L. (2020) A systematic exploration of satellite radar coherence methods for rapid landslide detection. *Natural Hazards and Earth System Sciences*, 20, 3197–3214. doi:10.5194/nhess-20-3197-2020

Copernicus Emergency Management Service (2026) EMSR927: Flood in Nepal. Rapid Mapping activation, 26 August 2026. https://mapping.emergency.copernicus.eu/activations/EMSR927/

Dini, B., Lacroix, P. and Doin, M.-P. (2026) Beyond and beneath displacement time series: towards InSAR-based early warnings and deformation analysis of the Achoma landslide, Peru. *Natural Hazards and Earth System Sciences*, 26, 863–879. doi:10.5194/nhess-26-863-2026

Faillettaz, J., Funk, M. and Vincent, C. (2015) Avalanching glacier instabilities: review on processes and early warning perspectives. *Reviews of Geophysics*, 53, 203–224. doi:10.1002/2014RG000466

Gruber, S., Fleiner, R., Guegan, E., Panday, P., Schmid, M.-O., Stumm, D., Wester, P., Zhang, Y. and Zhao, L. (2017) Review article: inferring permafrost and permafrost thaw in the mountains of the Hindu Kush Himalaya region. *The Cryosphere*, 11, 81–99. doi:10.5194/tc-11-81-2017

Guo, L., Xu, J., Wang, Y., Hu, Y., Peng, F., Sun, Y., Dian, J., Jiang, D., Li, X., Che, T., Chen, F., Qi, Y., Cao, Z., Li, J., Feng, M., Zhang, B., Chen, F. and Li, X. (2026) Progressive entrainment transformed a high-elevation ice–rock avalanche in Nepal into the 26 August debris flow in Gyirong, Xizang. *Chinese Science Bulletin*. doi:10.1360/CSB-2026-1255

HiRISK (2026) *Rapid Hazard Assessment Report No. NP3: Rasuwa Flood.* Liu, Q., Khatri, A., Lord, A., Ghouli, M., Thapa, N., Steiner, J., Immerzeel, W. W. and Allen, S. Asian Mountain Academic Alliance, Stimson Center and Institute of Mountain Hazards and Environment, Chinese Academy of Sciences, 28 August 2026.

Jacquemart, M. and Tiampo, K. (2021) Leveraging time series analysis of radar coherence and normalized difference vegetation index ratios to characterize pre-failure activity of the Mud Creek landslide, California. *Natural Hazards and Earth System Sciences*, 21, 629–642. doi:10.5194/nhess-21-629-2021

Kirschbaum, D., Watson, C. S., Rounce, D. R., Shugar, D. H., Kargel, J. S., Haritashya, U. K., Amatya, P., Shean, D., Anderson, E. R. and Jo, M. (2019) The state of remote sensing capabilities of cascading hazards over High Mountain Asia. *Frontiers in Earth Science*, 7, 197. doi:10.3389/feart.2019.00197

Li, R. (2026) When a high-mountain slope failure cascades downstream: reconstructing the 26 August 2026 Gyirong mixed rock–ice disaster. *arXiv* 2609.04563 [physics.ao-ph].

Mani, P., Allen, S., Evans, S. G., Kargel, J. S., Mergili, M., Petrakov, D. and Stoffel, M. (2023) Geomorphic process chains in high-mountain regions — a review and classification approach for natural hazards assessment. *Reviews of Geophysics*, 61, e2022RG000791. doi:10.1029/2022RG000791

NDRRMA (2026) *Rasuwa Flood: Search, Rescue and Relief Update*, 9 September 2026, 18:00 NPT. National Disaster Risk Reduction and Management Authority, Ministry of Home Affairs, Government of Nepal, Singhadurbar, Kathmandu. https://www.ndrrma.gov.np

Sah, A. K. (2026) No detectable precursor in Sentinel-1 backscatter before the 26 August 2026 Langtang Lirung rock–ice avalanche, Nepal. *EarthArXiv*. doi:10.31223/X59N5N

Shugar, D. H., Jacquemart, M., Shean, D. et al. (2021) A massive rock and ice avalanche caused the 2021 disaster at Chamoli, Indian Himalaya. *Science*, 373, 300–306. doi:10.1126/science.abh4455

Tiwari, A., Sain, K., Kumar, A., Tiwari, J., Paul, A., Kumar, N., Haldar, C., Kumar, S. and Pandey, C. P. (2022) Potential seismic precursors and surficial dynamics of a deadly Himalayan disaster: an early warning approach. *Scientific Reports*, 12, 3733. doi:10.1038/s41598-022-07491-y

UNOSAT (2026) Mudflow/rockflow impact assessment in Rasuwa and Nuwakot districts, Bagmati Province, Nepal, as of 26–27 August 2026; and Satellite-detected newly formed barrier lakes following an ice–rock avalanche in Rasuwa district, Nepal, as of 28 August 2026. https://www.unosat.org/products

US Geological Survey (2026) ANSS Comprehensive Catalog, search of the Nepal–China border region for the thirty days preceding 26 August 2026. Events us7000tbwb and us7000tc90, retrieved 8 September 2026. Query result archived with the analysis code.

Van Wyk de Vries, M., Bhushan, S., Jacquemart, M., Deschamps-Berger, C., Berthier, E., Gascoin, S., Shean, D. E., Shugar, D. H. and Kääb, A. (2022) Pre-collapse motion of the February 2021 Chamoli rock–ice avalanche, Indian Himalaya. *Natural Hazards and Earth System Sciences*, 22, 3309–3327. doi:10.5194/nhess-22-3309-2022

Zhuang, Y., Dawadi, B., Steiner, J., Dash, R. K., Bühler, Y., Munch, J. and Bartelt, P. (2024) An earthquake-triggered avalanche in Nepal in 2015 was exacerbated by climate variability and snowfall anomalies. *Communications Earth & Environment*, 5, 465. doi:10.1038/s43247-024-01624-z

---

Supplementary Material

Spring snowpack condition in the Langtang, 2017–2026

Companion to *Calibrated detection limits in routine Sentinel-1 products 50.6 hours before the Langtang Lirung rock–ice avalanche, Nepal*.

This section reports a separate analysis asking whether the months preceding the failure were anomalous in the Langtang, and if so in what respect. It is placed in supplementary material because its result is a null with respect to the failure: the condition it identifies is regional rather than slope-specific, it had closed before July, and a year with an indistinguishable signature produced no failure.

The analysis is reported here in the order it was carried out, including a prediction that failed and two statistical claims that were withdrawn. That ordering is deliberate. The interpretation offered at the end was reached after seeing part of the data, and a reader cannot weigh it without knowing which tests were specified in advance and which were not.

S1. Sites, windows and method

Thirteen sites in the Langtang: the source polygon and twelve terrain-matched controls, each a 500 m circle, drawn at least 2 km from the source and matched within 250 m in elevation, 10° in slope and 45° in aspect, under a fixed seed. All series were retrieved through the Sentinel Hub Statistics API over 2017 to 2026.

Three seasonal windows, fixed before any test: **winter** 1 January to 28 February, **spring** 1 March to 22 June, **summer** 1 July to 15 August. The winter and summer windows exist as controls. A calibration change, a geometry change or a processing artefact would move all three; a physical process confined to the melt season should move only the middle one.

S2. The radar observation

Regional mean spring cross-polarised backscatter in 2026 was **−18.03 dB**, against a 2017–2025 mean of −16.98 dB with a standard deviation of 0.415. That is **z = −2.52** and the lowest spring value in the ten-year record.

Lower backscatter has two candidate causes that are not distinguishable from a single channel: more snow, or wetter snow. The first test was designed to separate them using an independent sensor.

S3. The optical test, and the prediction that failed

Snow-covered fraction was computed from Sentinel-2 over the same thirteen sites and the same spring window, with snow defined as NDSI > 0.42 on cloud-free pixels, cloud rejection through the scene classification layer, and days discarded where less than 30 per cent of the polygon was clear. Spring is pre-monsoon, so optical coverage is far better than later in the year.

The prediction, stated in advance, was that 2026 would show less snow than usual — an early or prolonged melt being the simplest reading of low backscatter.

It did not. Every one of the thirteen sites returned a positive anomaly: source z = +0.44 (2017–2025 mean 0.805, 2026 0.840), controls mean z = +0.51 with standard deviation 0.25, none below zero.

The prediction failed in direction, and a first interpretation — that 2026 therefore had *more* snow than usual — was itself withdrawn on further inspection. Ranked against the decade rather than scored against its mean, 2026 places **fourth of ten** for snow cover, behind 2020, 2023 and 2019. The uniformly positive z arose because three recent years, 2022, 2024 and 2025, were unusually low and depressed the reference mean. Excluding the thin 2017 record, mean z falls to +0.40.

The defensible optical result is therefore that spring 2026 snow cover was ordinary.

S4. The residual

Across the ten years the two sensors track each other as expected — more snow, lower backscatter — at $r = -0.73$, $p = 0.017$. The year 2026 breaks that relationship: it sits at ordinary snow cover with record-low backscatter.

That residual is the observation this section exists to report. It is not explained by snow quantity, because snow quantity was measured independently and was ordinary.

Liquid water is the natural physical candidate, since an optical snow index detects that snow is present but cannot distinguish wet snow from dry, while absorption at C band rises sharply with liquid water content. **This explanation was reached after seeing the residual and is therefore not supported by anything reported above.** It was treated as a hypothesis requiring its own test.

S5. A pre-registered test of the wetness hypothesis

The hypothesis makes a prediction that snow quantity does not.

Liquid water attenuates along the propagation path. Cross-polarised return arises from multiple scattering through the snow volume and so accumulates substantially more path length than co-polarised return, which is dominated by the surface. Wetting should therefore suppress VH more than VV and drive the polarisation difference VH − VV more negative. A change in snow amount or grain size, without wetting, moves both channels together and leaves the difference approximately unchanged.

Two hypotheses, opposite predictions, one quantity — and that quantity was already present in the retrieved series, unexamined.

Prediction, recorded before the test: spring VH − VV anomalously negative in 2026; winter and summer unremarkable.

At the source polygon: spring **z = −2.71**, rank 1 of 10, with VH − VV at −13.17 dB against a nine-year mean of −11.91 and standard deviation 0.46. VH fell about 2.0 dB below normal while VV fell about 0.5 dB. Winter **z = +1.11**; summer **z = +1.18**.

Regionally, across the thirteen sites: spring VH − VV negative at all twelve controls as well as the source, with a regional value of −10.68 dB against a 2017–2025 mean of −10.06 and standard deviation 0.26, **z = −2.38**, rank 1 of 10. Winter mean +0.09; summer +0.98.

The seasonal controls behaved as they had to for the result to mean anything. An instrumental or processing cause would have widened all three windows. Only spring moved.

S6. Statistics, corrected

Two claims made during the analysis were withdrawn, both for the same reason.

A sign test across thirteen sites was reported at $p \approx 0.0002$, and a related counting argument at $p = 0.0003$. Both treat the sites as independent observations. They are not: the sites lie within roughly 15 km of one another and share the same weather, so they agree because they must. The mean inter-site correlation of spring anomalies is $r = 0.559$, giving an effective sample size of

$$n_{\text{eff}} = \frac{13}{1 + 12 \times 0.559} = 1.69$$

Thirteen sites carry approximately 1.7 sites' worth of independent information. With one region and ten years of record, the floor for a rank-based test is $p = 0.10$, and no test on this data can do better. All p-values quoted during the analysis and below that floor are withdrawn.

The regional agreement across sites should therefore be read as evidence that the signal is *regional in extent*, which was its purpose, and not as replication.

S7. Two results that count against a causal reading

Both come from tests designed to give the causal reading a chance.

The slope that failed is not distinguishable from its neighbours. Ranked on the spring anomaly, the source polygon places second of thirteen. One control site, ctrl06, was more extreme in spring 2026 and is still standing.

A year with an indistinguishable signature produced no failure. On the spring-minus-winter contrast, 2019 gives −2.61 against 2026's −2.62 — a difference of one hundredth of a decibel. The 2019 melt trough was the earliest in the record, at day 114 against 2026's day 113. Whatever spring 2026 was, spring 2019 was the same, and no rock–ice avalanche followed it. (The 2019 lowland flooding in the Terai is monsoon inundation hundreds of kilometres downstream in July, a different phenomenon, and does not restore the link.)

S8. The ten-year amplitude climatology

The companion paper, Sah (2026), attributes a candidate cross-polarised trend to a delayed seasonal transition, quantified against a single comparison year, 2025, as a deficit of approximately 3 dB.

Extending that comparison to the full record shows 2025 to have had the **latest melt trough of the ten years**, so it is an unrepresentative baseline and the deficit measured against it overstates the departure. Against the 2017–2025 median the deficit is approximately 1.2 dB, and across the 29 June to 16 August analysis window 2026 lies **on** the climatological median.

This strengthens rather than weakens the original conclusion. The seasonal explanation no longer rests on one comparison year, and the analysis window in which the candidate trend appeared turns out to be an ordinary one.

S9. What this section supports

The Langtang had an anomalously wet spring snowpack in 2026: record-low cross-polarised backscatter with ordinary snow cover, and a polarisation difference that widened to a decade record confined to the melt season, consistent with a mechanism stated in advance and tested against seasonal controls.

The condition was regional, not slope-specific. It had closed by July. The slope that failed was not the most extreme site. A year with an indistinguishable signature produced no failure. The summer preceding the collapse was ordinary by the amplitude climatology of Section S8.

Snowpack anomalies in this valley have been implicated in avalanche behaviour before. Zhuang et al. (2024) find that the 2015 earthquake-triggered avalanche in the Langtang was exacerbated by snowfall anomalies and climate variability. That is a different case from the one examined here, since a trigger was present in 2015 and none was in 2026, but it establishes the snowpack of this valley as a quantity worth measuring rather than assuming.

The sequence is real and the mechanism is defensible. Whether the wet spring contributed to the failure is untested here, and with one region, one event and ten years of record it is probably untestable. Establishing generality would require the same analysis across several valleys and several failures, which is beyond the scope of this paper.

S10. Data and code

Series were retrieved through the Sentinel Hub Statistics API using `control_test.py` (radar, thirteen sites), `pol_test.py` (polarisation difference) and `s2_snow.py` (optical snow fraction), archived with the derived series `control_test_series.csv` and `pol_test_series.csv`. Contains modified Copernicus Sentinel data 2017–2026.